Modeling thermal inkjet and cell printing process using modified pseudopotential and thermal lattice Boltzmann methods

Salman Sohrabi and Yaling Liu

Phys. Rev. E **97**, 033105 — Published 12 March 2018

DOI: 10.1103/PhysRevE.97.033105

Modeling Thermal Inkjet and Cell Printing Process Using Modified Pseudopotential and Thermal Lattice Boltzmann Methods

Salman Sohrabi
Lewis-Sigler Institute for Integrative Genomics
Princeton University, Princeton, NJ 08544, USA
Sohrabi@Princeton.edu

Yaling Liu[1]
Department of Mechanical Engineering & Mechanics
Bioengineering Program
Lehigh University, Bethlehem, PA 18015, USA
Yal310@lehigh.edu

Abstract

Pseudopotential Lattice Boltzmann methods (LBM) can simulate phase transition in high-density ratio multiphase flow systems. If coupled with thermal LBM through equation of state, it can be used to study instantaneous phase transition phenomena with high temperature gradient where only one set of formulations in LBM system can handle liquid, vapor, phase transition, and heat transport. However, at lower temperatures unrealistic spurious current at interface introduce instability and limit its application in real flow system. In this study, we proposed new modifications to LBM system to minimize spurious current which enables us to study nucleation dynamic at room temperature. To demonstrate the capabilities of this approach, thermal ejection process is modeled as one example of a complex flow system. In inkjet printer, a thermal pulse instantly heats up the liquid in microfluidic chamber and nucleate bubble vapor providing pressure pulse necessary to eject droplets at high speed. Our modified method can present a more realistic model of explosive vaporization process since it can also capture high temperature/density gradient at nucleation region. Thermal inkjet technology has been successfully applied for printing cells, but cells are susceptible to mechanical damage or death as they squeeze out of nozzle head. To study cell deformation, spring network model, representing cells, is connected to LBM through immersed boundary method. Looking into strain/stress distribution of cell membrane at its most deformed state, it is found that high stretching rate effectively increase rupture tension. In other word, membrane deformation energy is released thorough creation of multiple smaller nanopores rather than big pores. Overall, concurrently simulating multiphase flow, phase transition, heat transfer, and cell deformation in one unified LB platform, we were able to provide a better insight into bubble dynamic and cell mechanical damage during printing process.

Keywords: Pseudo-potential Lattice Boltzmann Method, Phase transition, Inkjet printing, Bubble nucleation, Cell membrane, Thermal Lattice Boltzmann Method, Spring connected network model, Droplet ejection.

---

[1] **Corresponding author.*
Postal address: 19 Memorial Dr W, Packard Lab, Lehigh University, Bethlehem, PA 18015
E-mail address: yal310@lehigh.edu
Electronic Supplementary Information (ESI) available: [Two multimedia files are provided as supplementary information].

1. Introduction

Different from conventional computational fluid dynamics methods [1-4], Lattice Boltzmann method (LBM) is based on mesoscopic kinetic equations in which the collective behavior of the particle distribution function (PDF) is used to simulate the continuum mechanics of the system [5, 6]. LBM has many advantages such as easy implementation of various physical phenomena and fully parallel algorithms [7]. Among various LB methods, pseudopotential model is simpler and more efficient in simulating high-density ratio multiphase flow system [5]. It also has lower computation cost compared to interface capturing methods such as Volume-of-Fluid (VoF) and level set methods [8]. The Shan and Chen (S–C) model [9] and the free energy model by Swift et al. [10] are two major pseudopotential LBMs. Single-component pseudopotential LBM is capable of simulating phase transition through incorporation of the non-ideal equation of state (EOS) such as Carnahan-Starling, Peng-Robinson (P–R), van der Waals, and Redlich-Kwong [8]. Among them, P–R EOS are proven to have the best thermodynamic consistency[5].

The stability issue is the main setback limiting the application of the pseudopotential model to most of real multiphase flow systems with high density ratio and phase transition. The major source of instability is non-zero vortex-like fluid velocity in the vicinity of phase interface which indicates the deviation from the real physical situation [11]. The so-called spurious currents drastically increase at lower temperatures (high density ratios). Therefore, achieving a stable solution at room temperature is challenging. The main criteria to assess pseudopotential LB models is maximum achievable density ratio, or lowest realizable temperature. Various EOSs and formulations for interparticle interaction forces have been tested to increase stability [8].

Using P−R EOS, exact difference method, and new scheme for derivation of interparticle interaction force, Gong and Cheng [8] reported lowest achievable temperature of $0.58T_c$. Later, Kupershtokh et al. [12] overcame this limitation and were able to achieve liquid to vapor density ratios as big as 10^7. Anjie Hu [7] furthered this approach to demonstrate the feasibility of reaching temperature as low as $0.2T_c$ with density ratio of 10^9. However, their major setback in this approach is compromising surface tension and increase in interface thickness. In these studies, models are evaluated by comparing the coexistence curves obtained from the simulation with the theoretical one predicted by the Maxwell equal-area construction. To the best of our knowledge, these pseudopotential models has not yet been applied to the real multiphase flow systems at ambient temperature.

In this study, we used a reliable and stable modified formulations to minimize spurious current at different saturation temperatures. Thermal LBM is also coupled with pseudopotential model evolving at the same paces as particle distribution function. The spatial and temporal changes of temperature are implemented through EOS while flow information is used to update temperature distribution. To demonstrate the capabilities of proposed model, our modified formulations are used to simulate thermal injection process.

Inkjet printers are capable of delivering micro droplets at low manufacturing cost in applications such as additive manufacturing, bioprinting, and cell patterning [13, 14]. Due to the low cost and high quality, thermal-type inkjet printers are more popular [15]. In thermal bubble injection, 3μs-6μs width pulse wave with frequency of 1kHz-5kHz is applied to instantly heat the liquid in reservoir and nucleate bubble vapor providing the pressure pulse necessary to eject drop of ink out of the nozzle [16]. The size of droplets varies according to the applied temperature gradient, frequency of current pulse, and ink viscosity. To visualize explosive vaporization process, complex formulations are needed to capture phase separation/transition as well as heat transfer at liquid–vapor interface [16]. Because of high pressure in superheated vapor bubble, compressibility effect should be also included during instantaneous nucleation [17]. Due to this level of complexity, realistic simulation of thermal injection process can be challenging.

Both level-set and VoF methods have been applied in simulations of droplet ejection [16-19]. These methods treat vapor region as a cavity and adopt Clausius–Clapeyron equation to predict bubble pressure [16]. However, in coupled pseudopotential-thermal LBM, only heat pulse is needed to be applied on boundary and everything else, e.g.

bubble nucleation, growth and collapse, are being taken care of by one set of formulations. The simplicity of our approach distinct it from other conventional interface capturing methods [20-23].

Inkjet printing has been successfully applied for printing sophisticated patterns of biomolecules on various substrates [14, 24, 25]. However, there are concerns that printing process may cause cell damages or death. In bioprinters, bio-ink in cartridge is forced through a microfluidic chamber to an output orifice. Among different printing methods, cell membrane are more likely to be damaged in piezoelectric inkjet printers due to range of frequencies used [24, 26]. Although the temperature is locally increased to 300°C for a few microseconds in thermal inkjet printers, the overall temperature only rise 4–10°C and the average cell viability of 90% can be achieved [26]. In this study, we specifically are looking into cell deformation and membrane mechanical damage as it squeezes out of thermal inkjet print head. To incorporate cell body, spring network (SN) model is coupled with pseudopotential LBM through immersed boundary method [27-29]. By coupling these models, the injection dynamic and cell deformation at high speed can be visualized. In the following, first the proposed model is described and validated. Then, after discussing the results of injection simulation, cell deformation/damage is examined.

2. Method

In this study, pseudopotential LBM is used to model phase transition in high-density ratio flow systems [5]. Moreover, thermal LBM is utilized to solve energy equation. To incorporate cell in particulate flow [27, 28], SN model is also coupled with pseudopotential LBM. In what follows, these methods and relevant formulations are discussed.

Pseudopotential LBM

In standard lattice Boltzmann, Bhatnagar-Gross-Krook (BGK) scheme describes the evolution of PDF, $f_i(x,t)$, at phase space $(x,\vec{c_i})$ at time t, where $\vec{c_i}$ is the discretized velocity. The LBM dynamics involve streaming and collision steps

$$f_i(x+\Delta t\vec{c_i},t+\Delta t) = f_i(x,t) - \frac{1}{\tau_f}\left[f_i(x,t) - f_i^{eq}(x,t)\right] + \Delta f_i(x,t) \quad (1)$$

$$f_i^{eq} = \omega_i \rho\left[1 + \frac{e_i.u}{c_s^2} + \frac{(e_i.u)^2}{2c_s^4} - \frac{u^2}{2c_s^2}\right] \quad (2)$$

where $f_i^{eq}(x,t)$ is its corresponding equilibrium PDF, τ_f is the PDF relaxation time, c_s is the speed of sound in LB scheme, and i is the number of discrete particle velocities. Macroscale density and velocity can be obtained as

$$\rho(x,t) = \sum_i f_i(x,t) \quad (3)$$

$$\rho(x,t)\,\vec{u}(x,t) = \sum f_i(x,t)\vec{c_i} \quad (4)$$

The weighting factor and discrete velocity for D3Q19 lattice models are given as

$$e_i = \begin{cases} (0,0,0) & \alpha = 0; \\ (\pm1,0,0)c, (0,\pm1,0)c, (0,0,\pm1)c, & \alpha = 1,2,\dots,6; \\ (\pm1,\pm1,0)c, (\pm1,0,\pm1)c, (0,\pm1,\pm1)c, & \alpha = 7,8,\dots,18; \end{cases} \quad (5)$$

$$\omega_i = \begin{cases} 1/3 & \alpha = 0; \\ 1/18 & \alpha = 1,2,\dots,6; \\ 1/36 & \alpha = 7,8,\dots,18; \end{cases} \quad (6)$$

The total force acting on a fluid particle in multiphase flow may origin from different sources

$$F_T = F_{int} + F_s + F_g + F_{cell} \quad (7)$$

where F_s is the solid–fluid interaction force, F_{int} is the inerparticle interaction forces, F_{cell} is the cell–fluid interaction force, and F_g represents gravitational force. In this study, exact difference method (EDM) is used to incorporate the force term into eqn. 1 through Δu. $\Delta f_i(x,t)$ in EDM can be calculated as

$$\Delta f_i(x,t) = f_i^{eq}(\rho(x,t), u+\Delta u) - f_i^{eq}(\rho(x,t),u), \quad (8)$$

where $\Delta u = F_T.\Delta t/\rho$ is the velocity change due to the body force during lattice time step (δ_t). EDM was proposed by Kupershtokh and Medvedev [12] where the body force term is added directly to the right-hand side of eqn. 1 and

there is no need to discretize the body force. There are also other methods to incorporate force term such as velocity shifting method and discrete force method [8]. More detail information concerning these approaches can be found in [8] where it is shown that EDM has better accuracy and stability. In the following, all forces acting on particulate flow are discussed in detail.

Interparticle interaction forces

Microscopically, the segregation of a fluid system into different phases is due to the interparticle forces, see eqn. 7. In the pseudopotential model, the interparticle interaction force, F_{int}, is responsible for phase separation. In this study, modified S-C's interparticle interaction force scheme is used.

$$F_{int}(\mathrm{x}) = -\beta c_0 g\, \psi(x)\nabla\psi(x) - (1-\beta)c_0 g\, \nabla\psi(x)^2/2 \tag{9}$$

where β is the weighting factor; c_0 is 6.0 for D3Q19 lattice structure; and $\psi(x)$ is effective mass which reflects the intensity of the interparticle interaction. The value of $\beta = 1.16$ is optimized to best match Maxwell construction [30]. Eqn. 9 can be discretized as

$$F_{int}(x) = -\beta\psi(x)\sum_{x'} G(x,x')\psi(x')(x'-x) - \frac{1-\beta}{2}\sum_{x'} G(x,x')\psi^2(x')(x'-x) \tag{10}$$

where $G(x,x')$ and $\psi(x)$ are given by

$$G(x,x') = \begin{cases} \mathrm{g}_1, & |x'-x| = 1 \\ \mathrm{g}_2, & |x'-x| = \sqrt{2} \\ 0, & otherwise \end{cases} \tag{11}$$

$$\psi(\rho) = \sqrt{\frac{2(p-\rho c_s^2)}{c_0 g}} \tag{12}$$

with $\mathrm{g}_1 = \mathrm{g}$, $\mathrm{g}_1 = g/2$ for D3Q19 scheme. In multi-component S-C model, eqn. 12 is simplified as $\psi(\rho) = \rho_0[1 - \exp(-\rho/\rho_0)]$ which gives a nonmonotonic pressure-density relationship. In this case, the temperature is constant and equal $T = -1/g$ in lattice unit. Also, the role of pressure is dictated through g while $\rho_c = \rho_0 ln2$ and $\mathrm{g}_c = -2/(9\mathrm{g}_0)$. Hence, for $g < \mathrm{g}_c$ two densities of the same material can coexist at a single pressure and temperature. However, by changing the form of $\psi(\rho)$, different equation of state can be theoretically obtained. In this study, Peng–Robinson (P–R) equation of state which is more accurate and popular for water is used

$$p = \frac{\rho RT}{1-b\rho} - \frac{a\rho^2\varepsilon(T)}{1+2b\rho-b^2\rho^2} \tag{13}$$

where $\varepsilon(T) = [1 + (0.37464 + 1.54226\omega - 0.26992\omega^2)]^2$, with $\omega = 0.344$ being the acentric factor for water. By setting first and second derivatives of the pressure to zero, $a = 0.4572\, R^2T_c^2/P_c$ and $b = 0.0778\, RT_c/P_c$ can be derived. Since lattice sound speed is $c_s = \sqrt{3RT_c} = 1/\sqrt{3}$, by choosing $R = 1$, $a = 2/49$, and b= $2/21$, critical temperature, pressure, and density in lattice unit can be accordingly calculated as $T_c = 0.0729$, $P_c = 0.0596$, $\rho_c = 2.3382$.

Solid–fluid interaction force

Interaction force, eqn. 7, between the solid and fluid is given by

$$F_s(x) = -\left(1 - e^{-\rho(x)}\right)\sum_i g_s\omega_i s(x + e_i\delta_t).e_i\delta_t \tag{14}$$

where g_s is the fluid–solid interaction and can be adjusted for proper contact angle. The indicator function, $s(x)$, is equal to 1 and 0 when x is in solid and fluid, respectively. Furthermore, the gravity force, eqn. 7, is given by

$$F_g(x) = \mathrm{G}.[\rho(x) - \rho_{ave}] \tag{15}$$

where G is the acceleration of gravity and ρ_{ave} is the average density at each time step.

Thermal Lattice Boltzmann method

Temperature in equation of state can be derived by solving energy equation [31]

$$\frac{\partial T}{\partial t} + \nabla.(U\mathrm{T}) = \nabla.(\alpha\nabla\mathrm{T}) + \phi \tag{16}$$

where $\alpha = \frac{\lambda}{\rho c_v}$ is the thermal diffusivity. To solve eqn. 16 by thermal LBM, a second set of distribution function is introduced,

$$T(x,t) = \sum_i g_i(x,t) \tag{17}$$

Similarly, the temperature distribution function evolves by

$$g_i(x + \Delta t\vec{c_i}, t + \Delta t) - g_i(x,t) = -\frac{1}{\tau_T}\left[g_i(x,t) - g_i^{eq}(x,t)\right] + \Delta t\omega_i\phi \tag{18}$$

where τ_T is thermal the relaxation time, ϕ the source term responsible for phase change and $g_i^{eq}(x,t)$ is the equilibrium temperature distribution function given by

$$g_i^{eq} = \omega_i\rho\left[1 + \frac{e_i.u}{c_s^2}\right] \tag{19}$$

Source term in eqn. 16 represent heat storage/release during phase transition process. To derive Φ in term of p, T and ρ, entropy balance equation, $\rho T\frac{ds}{dt} = \nabla.(\lambda\nabla T)$, is used in conjunction with thermodynamic relations [32]. Gong and Cheng [32] demonstrated that entropy balance equation can be rewritten in the form of heat transport equation where the last two terms represent the source term responsible for phase change. Finally, they derived a simplified equation for Φ which were written as

$$\phi = T\left[1 - \frac{1}{\rho c_v}\left(\frac{\partial p}{\partial T}\right)_v\right]\nabla.U \tag{20}$$

where c_v is specific heat capacity.

Model Parameters

The kinematic viscosity and thermal diffusivity in lattice unit are given by

$$\upsilon_{LB} = c_s^2\left(\tau_P - \frac{1}{2}\right)\Delta t_{LB} \tag{21}$$

$$\alpha_{LB} = c_s^2\left(\tau_T - \frac{1}{2}\right)\Delta t_{LB} \tag{22}$$

where τ_P and τ_T are relaxation parameters in pseudopotential and thermal LBM, respectively. Reynolds and Prandtl dimensionless numbers bring physical parameters to lattice units and can be defined as

$$Re = \frac{U_{Phy}L_{char}}{\upsilon_{Phy}} = \frac{U_{LB}L_{LB}}{\upsilon_{LB}} \tag{23}$$

$$Pr = \frac{\upsilon_{phy}}{\alpha_{phy}} = \frac{2\tau-1}{2\tau_T-1} \tag{24}$$

To convert physical parameters to lattice units, characteristic time, length, mass, and temperature should be calculated first. Characteristic length and time scales are given as

$$U_{phy} = \frac{L_{phy}}{t_{phy}} = \frac{N_{mesh}\times\Delta x_{char}}{N_{iter}\times\Delta t_{char}}$$
$$U_{LB} = \frac{L_{LB}}{t_{LB}} = \frac{N_{mesh}\times\Delta x_{LB}}{N_{iter}\times\Delta t_{LB}} \tag{25}$$

where N_{mesh} is the number of mesh in characteristic length scale; N_{iter} is the number of iteration during characteristic time scale. Generally, we assume $\Delta t_{LB} = 1$, $\Delta x_{LB} = 1$, and $c_s = 1/\sqrt{3}$. Using discussed relations, physical time step can be derived as

$$\Delta t_{phy} = \frac{L_{phy}^2}{N_{mesh}^2}\times\frac{(\tau_P-0.5)/3}{\upsilon_{Ref}} \text{ or } \Delta t_{phy} = \frac{L_{phy}^2}{N_{mesh}^2}\times\frac{(\tau_T-0.5)/3}{\alpha_{Ref}} \tag{26}$$

It can be seen that by setting L_{phy}, N_{mesh}, and kinematic viscosity (or thermal diffusivity), time step in physical system can be simply calculated. The acceptable range for both relaxation times are between 0.5 and 2.The closer it get to 0.5, more unstable LB simulation will be. Additionally, pseudopotential and thermal LBM are needed to evolve in the same pace. We also know that the value of kinematic viscosity and thermal diffusivity may vary orders of magnitude depending on density (vapor and liquid) and temperature at different regions of computational domain. To address these issues, maximum kinematic viscosity (or thermal diffusivity) within desired temperature range

should be identified first and set $\tau = 1.99$. Based on this assumption, characteristic time and length in both physical and lattice units can be accordingly calculated. Furthermore, critical density and temperature in lattice unit are set 0.0729 and 2.3382 in pseudopotential LBM. Thus, by using $\rho_c = 322\frac{kg}{m^3}$ and $T_c = 647.096$ °K in physical system, characteristic mass and temperature can also be calculated and then used to convert all other physical parameters. Physical parameters at liquid-vapor interface are estimated as

$$\chi = \chi_{liquid} \cdot \frac{\rho - \rho_{vapor}}{\rho_{liquid} - \rho_{vapor}} + \chi_{vapor} \cdot \frac{\rho_{liquid} - \rho}{\rho_{liquid} - \rho_{vapor}} \quad (27)$$

Viscosity and thermal diffusion are temperature/density dependent physical properties. Thus, their values in physical unit constantly change during phase transition or temperature fluctuation. Thus, it is imperative to adjust their value in lattice unit accordingly. We will be use these fixed characteristic scales. For instance, the temperature rise in computational domain will result in decrease of thermal diffusion. Thus, the value of τ_T should be subsequently updated because of this change.

Spring network model

Mechanical properties of cells depend on the mechanical properties of the subcellular components such as cytoplasm, nucleus, cell membrane, and cytoskeleton, as well as their distribution, linkage, and structure within the cell. Due to heterogeneous intracellular structures, proper modeling of cell mechanics is very challenging. Particular structures such as spring connected network model (SN) has been widely used for simulating blood cells [33-35]. In the case of regular cells, membrane and nuclear envelope can be modeled as a spring network while actin fiber are represented by a linear spring [36]. In SN, the membrane is composed of a set of vertex nodes $X_i, i \in \{1 \dots N_V\}$ that are connected by springs [36, 37] forming a two-dimensional triangulated network. Elastic resistances to changes in bending, stretching, and surface area can be implemented through potential energies.

$$V(\{x_i\}) = V_{in-plane} + V_{bending} + V_{area} + V_{volume} \quad (28)$$

The in-plane energy term characterizes the elastic energy stored in the membrane. The bending potential corresponds to bending stiffness of membrane while the last two potential term conserve volume and surface area of lipid bilayer. More detail information about these energy terms can be found in Refs. [33, 36, 38]. The nodal forces corresponding to the each energy can be calculated as $f_i = -\partial \mathrm{V}\{x_i\}/\partial x_i$. To avoid complexity, nuclear envelope and actin fibers are not considered in our current cell model.

Using Immersed Boundary method (IBM), parametric surface $X(s,t)$ exert a force density on the fluid, $F_c(x,t)$, to represent the effect of solid body [39, 40]. Similarly, the solid velocity, $u(X,t)$, will be interpolated from the local fluid nodes and will be used to update solid nodes [27, 41].

$$F_c(x,t) = \int f(s,t)\delta\big(x - X(s,t)\big)ds \qquad , u(X,t) = \int u(x,t)\,\delta(x - X(s,t))dx \quad (29)$$

$$\delta(r) = \begin{cases} \frac{1}{4}\left(1 + \cos\left(\frac{\pi r}{2}\right)\right) & -2 \le r \le 2 \\ 0 & otherwise \end{cases} \quad (30)$$

Our cell model is benchmarked with optical tweezer experimental data in our previous work [33, 41] where we studied red blood cell damage. In the same study, the deformation of RBC under pure shear flow is also investigated where the results for oscillation period agreed with experiments of Abkarian et al. [42].

Boundary conditions

In this study, Zou/He bounce back rules [43] is used to enforce non-slip wall boundary condition. Furthermore, constant surface temperature is applied using Dirichlet boundary condition.

$$g_i^*(x, t + \Delta t) = [\omega_i + \omega(-\Delta t\vec{c_i})]\mathrm{T}_{wall} - g(x, -\Delta t\vec{c_i}, t) \quad (31)$$

where T_{wall} is temperature at the wall. To apply heat pulse, Neumann boundary condition is utilized

$$g_i^*(x, t + \Delta t) = [\omega_i + \omega(-\Delta t\vec{c_i})](\textstyle\sum_i g_i(x,t) + Q_s/\mathrm{k}) - g(x, -\Delta t\vec{c_i}, t) \quad (32)$$

where $Q_s(W/m^2)$ is heat flux from heater resistor and k $(W/m.k)$ is thermal conductivity. At each node on heating element, temperature is used to first evaluate k at both phases, then eqn. 27 is used to estimate actual thermal

conductivity. Other model parameters such as kinematic viscosity, thermal diffusivity, and specific heat capacity are also strongly depend on temperature and are needed to be continuously updated in the same manner.

To calculate interparticle force, effective mass at all neighboring lattice nodes should be calculated first. But eqn. 10 can no longer be used for nodes on the wall. However, it can be modified in a way that eliminate the necessities for tedious computations. Calculated effective mass for nodes inside domain can be simply copied to ghost lattice points on the other side of wall as shown in Fig. 1. Thus, eqn. 10 can be modified as

(33)

where represents correction coefficient along axis. is one except for directions that have ghost lattice points in either directions ( ). It should be noted that the normal component of interparticle force at wall should also be zero. This condition at curved boundaries can be simply enforced through updating where is unit normal vector.

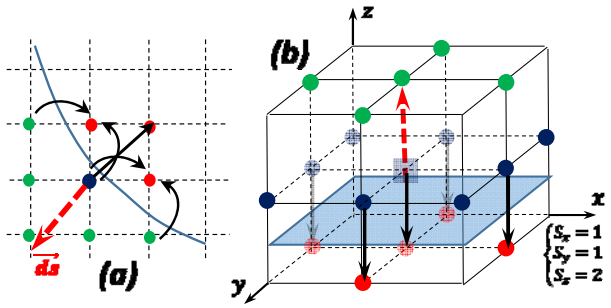

Fig. 1. Calculation of interparticle force on boundary nodes using ghost points (shown in Red).

3. Model Validation

The curve at subcritical temperature allows the coexistence of liquid and vapor densities at a single pressure and temperature. Gibbs free energy have equal values at liquid and vapor phases in equilibrium as shown in Fig. 2. This is the basic idea for Maxwell construction of EOS, where and are specific volume of saturated liquid and vapor, respectively. Using P–R EOS, system pressure versus densities can be plotted at different saturation temperatures as shown in Fig. 2. It can be seen that density ratio increases as temperature decrease, for instance at , the density ratio is .

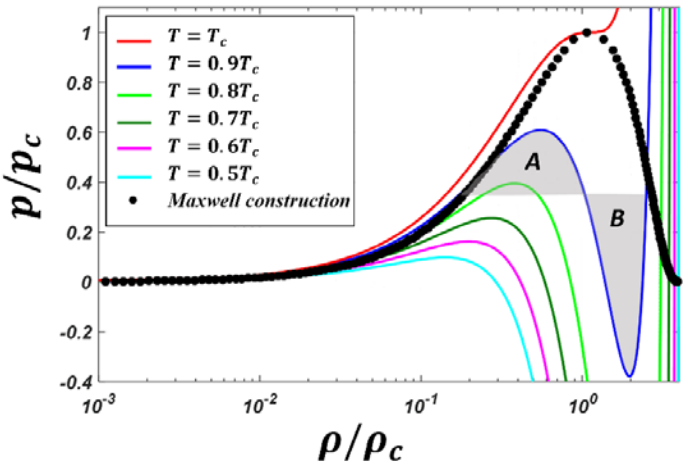

Fig. 2. Maxwell construction of Peng–Robinson (P–R) equation of state at various subcritical temperatures. Highest pressure at is shown with red solid line (dark grey) while lowest pressure at is shown in solid cyan line (light grey).

The stability issue is the main reason limiting the application of the pseudopotential model to most of the real multiphase flow systems at room temperature. The source of instability is spurious currents which almost exponentially increase as temperature decrease [8]. Among various pseudopotential multiphase models, Gong and Cheng [8] modified Yuan and Schaefer's formulation [5] and showed that they could be able to achieve a minimum temperature of $0.58T_c$ using P–R EOS and velocity shifting method. However, the spurious current is still high and the solution is very unstable. Additionally, the only way to achieve a stable solution at $0.58T_c$ is to gradually decrease temperature. These limitations made the application of this model without proper modification very challenging.

To address this issue, Kupershtokh et al. [12] proposed reduced equations of state to achieve density ratios as high as 10^7 using vdW and mKM[2] EOSs. Following similar principal, Anjie Hu et al. [7] investigated the effect of reduced parameter on spurious current and surface tension. In this approach, the pressure term can be modified as

$$\acute{p} = k'p = k'\left[\frac{\rho RT}{1-b\rho} - \frac{a\rho^2\varepsilon(T)}{1+2b\rho-b^2\rho^2}\right] \tag{34}$$

where $k \leq 1$ represents the reduced parameter. The value of reduced parameter does not influence the Maxwell construction of equations of state [7]. It should be noted that the introduced parameter effectively reduces spurious currents and enable us to simulate liquid-vapor density ratio as high as 10^9 when $k' = 0.01$ [7]. The temperature was fixed in these studies as opposed to our case where we plan to use thermal LBM to calculated temperature.

The stability of pseudopotential model can be evaluated by comparing the coexistence curves obtained from simulation with the theoretical one predicted by the Maxwell equal-area construction. To simulate the formation of a liquid droplets at a given temperature, initial density distribution at the center is set slightly higher than the rest of the domain. Periodic boundary conditions are imposed on all directions where $150 \times 150 \times 150$ lattice structure is chosen for computation. Particle and thermal relaxation times for both liquid and vapor phases are calculated as shown in Table 1. By using proper values for reduced parameter, magnitude of spurious current can be controlled. Simulations were carried out for 40,000 time steps to ensure that the steady state was reached. At the steady state, liquid droplets (with density ρ_l) surrounded by the vapor (with density ρ_g) are formed in computational domain as shown in Fig. 3. It is observed that our coupled pseudopotential-thermal model matches Maxwell construction perdition for P-R EOS.

Table 1. Model parameter in both lattice and reference units at different simulated temperatures.

T	τ^l	τ^v	τ_T^l	τ_T^v	ν_l^{Ref}	ν_v^{Ref}	α_l^{Ref}	α_v^{Ref}
$\mathbf{0.45}T_c$	0.502	1.970	0.5003	1.979	1.0×10^{-6}	6.27×10^{-4}	1.08×10^{-7}	6.31×10^{-4}
$\mathbf{0.5}T_c$	0.506	1.953	0.5014	1.526	5.5×10^{-7}	1.26×10^{-4}	1.22×10^{-7}	8.89×10^{-5}
$\mathbf{0.6}T_c$	0.527	1.966	0.515	1.459	2.5×10^{-7}	1.32×10^{-5}	1.33×10^{-7}	8.63×10^{-6}
$\mathbf{0.7}T_c$	0.528	1.973	0.522	1.109	1.7×10^{-7}	8.8×10^{-6}	1.36×10^{-7}	3.65×10^{-6}
$\mathbf{0.8}T_c$	0.701	1.925	0.697	1.205	1.3×10^{-7}	9.5×10^{-7}	1.31×10^{-7}	4.7×10^{-7}

[2] Kaplun_Meshalkin EOS

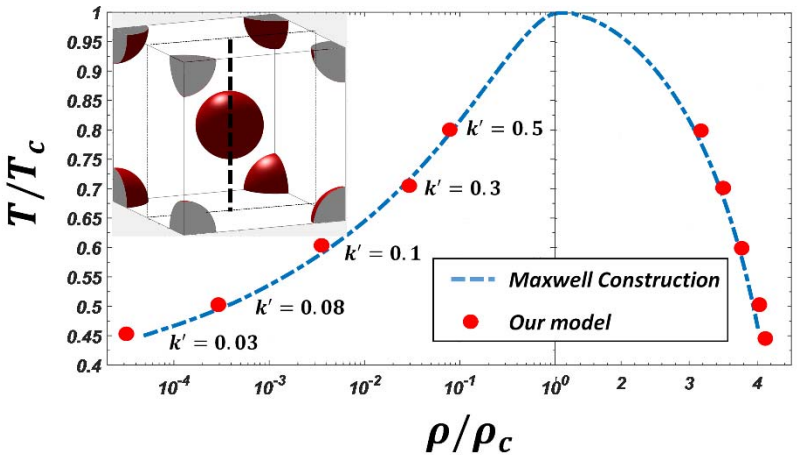

Fig. 3. Maxwell construction perdition for P-R EOS versus simulation results of our coupled pseudopotential-thermal model using reduced EOS. The relative density, , are demonstrated in two linear and logarithmic scales at right and left, respectively.

Mesh size is an important parameter influencing phase separation. To perform mesh dependency study, simulations with different mesh densities are carried out at with as shown in Fig. 4. For mesh size bigger than 120, vapor density solution matches the Maxwell construction prediction. Additionally, interface thickness decrease as mesh density increases. However, spurious current is not influenced by mesh density. Theoretically, the reduced parameter won't influence phase separation dynamic [7] and it should only decrease spurious current. Fig. 5 demonstrates the effect of reduced parameter on liquid and vapor densities. At constant temperature , the thickness of interface decreases to almost half by increasing from 0.05 to 0.1. However, high spurious current in case disturb uniform temperature distribution. On the other hand, at lower reduced parameter the interface thickness significantly increases, and one would need much more mesh node to acquire correct vapor density in saturated state.

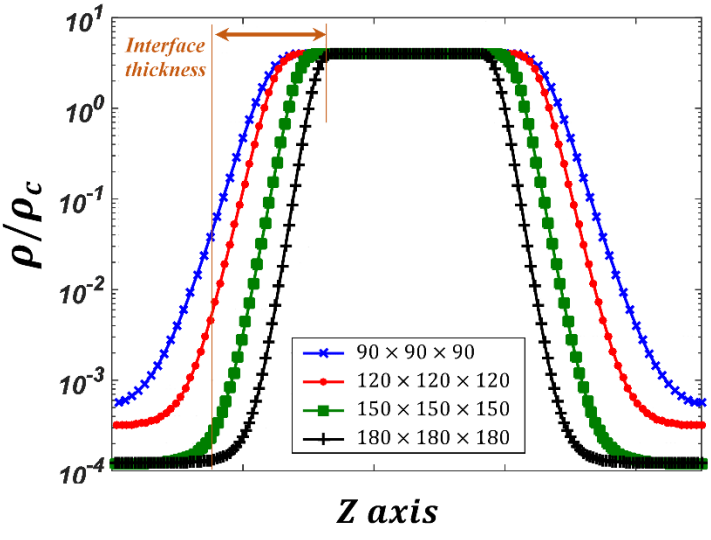

Fig. 4. Mesh dependency analysis of phase separation at . Relative density data along dotted line shown in Fig. 3.

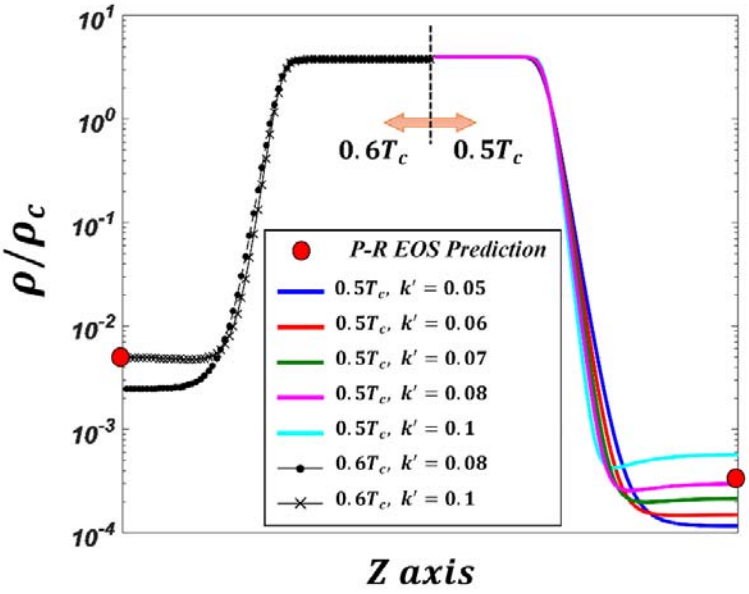

Fig. 5. Liquid-vapor separation for different reduced parameter. Mesh size is . From highest density to lowest density .

The effect of temperature and reduced parameter on maximum spurious current are also studied as shown in Fig. 6. It is observed that for , our results very well match with Gong and Cheng study for and [8]. As shown in Fig. 6, the spurious current at ( ) is no longer negligible compared to speed of sound, . High spurious current at interface generate unphysical temperature gradient. By keeping spurious current under ~0.03, cases with at and at are found to match Maxwell construction prediction better as shown in Fig. 5 and Fig. 6. For spurious currents lower than ~0.03, the magnitude of temperature fluctuation at interface is also negligible, . On the other hand, reduced parameter should be large enough to avoid very thick phase interface. Thus, choosing proper value for reduced parameter when modeling phase transition in a multi-phase flow is critical.

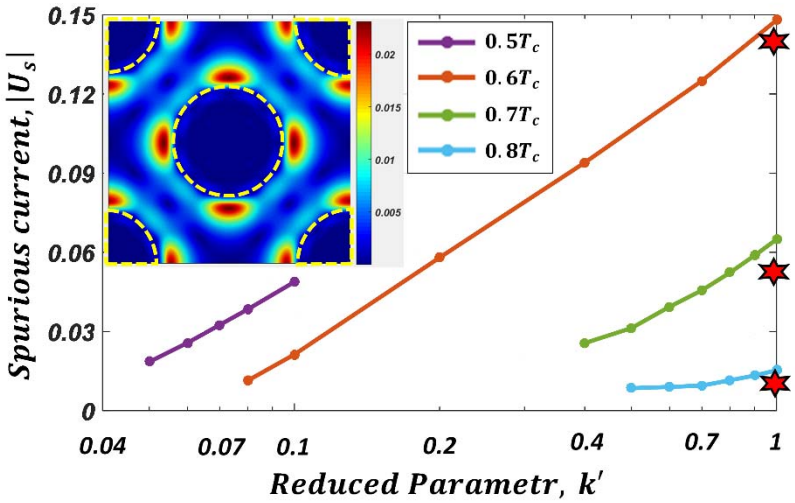

Fig. 6. Spurious current in lattice unit for various temperatures and reduced parameters. The red stars represent spurious current at using original pseudopotential formulation by Gong and Cheng [8]. and are colored violet (dark grey) and blue (light blue), respectively . The velocity distribution contours demonstrate unrealistic spurious current at phase interface.

To benchmark wall-fluid interaction, we have simulated droplet on a surface as shown in Fig. 7a-c. The liquid–solid interaction strength, , represents the strength of the intermolecular force between wall and fluid. By tuning , we can control the wettability of surface or in other word contact angle. The density distribution along z axis are also demonstrated for cases with different contact angles as shown in Fig. 7d. To demonstrate the capabilities of discussed approach, thermal ejection process is modeled as an example of a complex multiphase flow system.

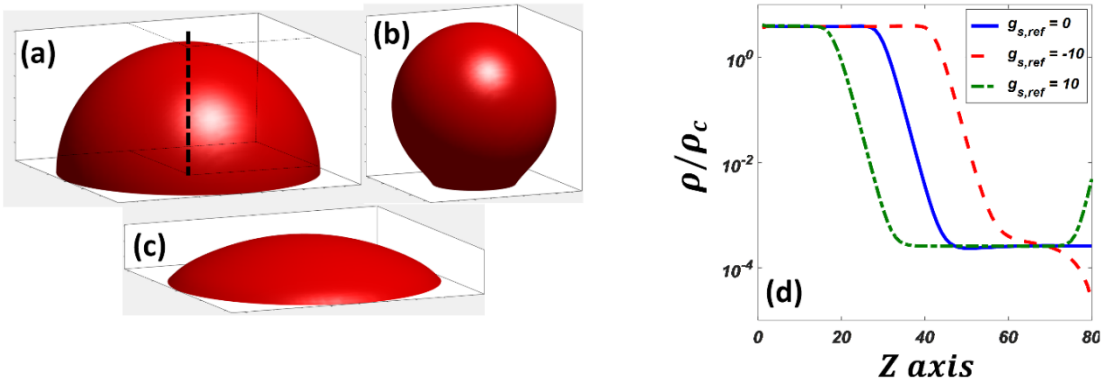

Fig. 7. Droplet on a surface for different liquid–solid interaction strengths, (a) , (b) , (c) . These simulations are carried out with initial temperature of with lattice nodes. (d) Relative density across dashed line for various liquid–solid interaction strengths.

4. Thermal inkjet printer

To simulate bio-printing process, the geometrical configuration of HP60 inkjet cartridge is used where cells are ejected through a narrow nozzle channel with a diameter of . The cross-section of HP60 nozzle plate and schematics of computational model are presented in Fig. 8a-b. Computational domain consists of lattice nodes and Zou/He bounce back rules[44] is applied at all surfaces. In HP60 inkjet cartridge, the heating resistors under each nozzle are stressed with a , pulse to boil the ink and eject the drop. This takes the resistor up to above the superheating point of water and creates an almost explosive vapor bubble that ejects the ink droplet at . For water at atmospheric pressure, nucleate boiling occurs at . However, the liquid in thermal inkjet printer begins to boil only when it is heated close to the superheat temperature of 580K. The reason is that the liquid is heated extremely quickly with heat flux as high as [16]. Thus, nucleation bubble instantaneously covers the surface of the heater in ~0.01ms where the bubble pressure can reach as high as ~8-12 MPa [16]. The bubble then collapses, and the ink cavity refills with liquid. The initial pressure and volume of the vapor bubble depend on firing conditions such as voltage pulse and liquid temperature.

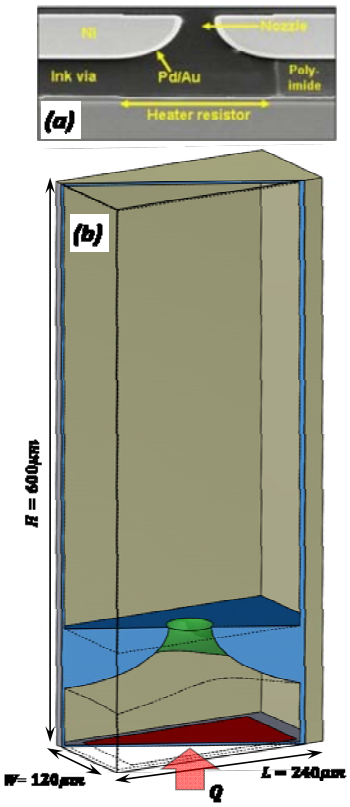

Fig. 8. (a) Cross-section of HP60 nozzle plate. (b) Schematics of microinkjet nozzle in computational model. Heating resistor is shown in Red.

Because the superheated vapor bubble behaves like a compressible fluid during grow and collapse cycle, it cannot be directly handled by incompressible flow solvers. To overcome this issue, the flow in the vapor domain is ignored in literature and vapor bubble is treated as a cavity so that the bubble can freely expand and shrink [45]. Thus, only the pressure information, force on the liquid surface, is passed onto fluid solver. However, due to high temperature and density gradient in the bubble region, bubble dynamic might be different from what has been previously realized [13, 16, 45-47]. Due to high dependency of local pressure, density and temperature on each other, EOS is needed to be directly implemented. Furthermore, the model should also be capable of simulating phase transition. Thus, our modified pseudopotential LBM coupled with thermal LBM can nicely capture the nucleation flow dynamics during injection process.

To simulate thermal injection process at ambient temperature, computational domain is needed to be initialized first where water and vapor phases are separated at the nozzle head. Initialization of thermal pseudopotential LBM is challenging since the simulation cannot be simply started by setting liquid and vapor densities at desired lattice nodes. The reason is that abrupt changes in density at interface instantly diverge the solution. One approach is starting simulation in higher temperature, e.g. $0.8T_c$, where solution is significantly more stable and then gradually decrease it. In this case, we may not be able to fully fill the reservoir with liquid or droplet may be created outside of the reservoir. To address this issue, we first set vapor density on all lattice nodes. Then the density of nodes inside reservoir are gradually raised to target liquid density as shown in Fig. 9.

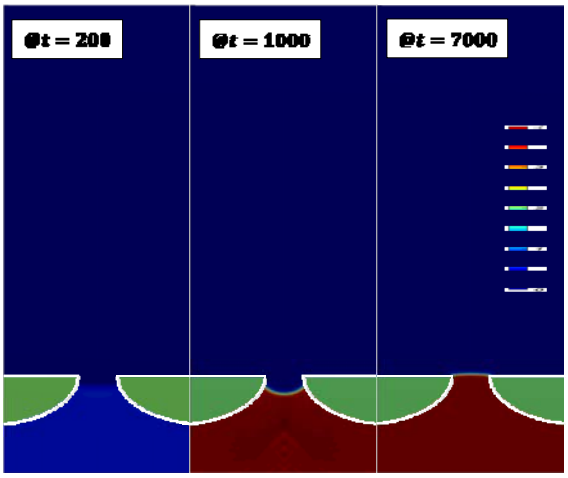

Fig. 9. Relative density distribution during initialization. marks in reference unit.

As discussed before, the reduced parameter is introduced to maintain the spurious current within acceptable range and avoid solution divergence. It is observed from Fig. 6 that different values of reduced parameter can be used at different saturation temperatures. Therefore, reduced parameter is assumed to linearly increase to one as the temperature reaches as shown in Fig. 10. By doing this, we managed to avoid high spurious current at nucleation region. Although the formulations used to incorporate phase transition, heat transfer, cell deformation, and solid-liquid-gas interaction in a curved geometry seems very complicated, the implementation in LB platform is relatively simple, see Fig. 11. After calculating interparticle interaction, wall, cell and gravity forces, PDFs undergo collision and stream steps. Then, by inputting heat flux at boundary and calculating phase transition term, thermal LBM is solved.

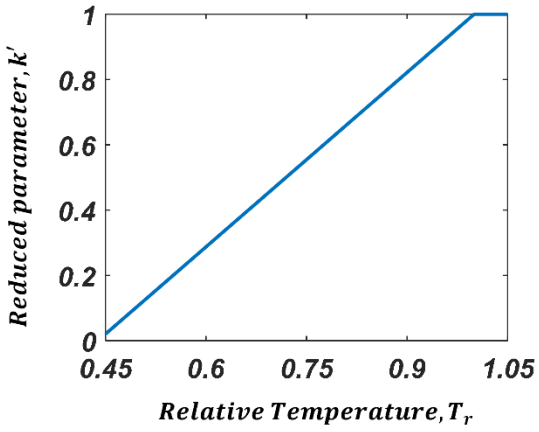

Fig. 10. Linear variation of reduced parameter versus relative temperature. equals at .

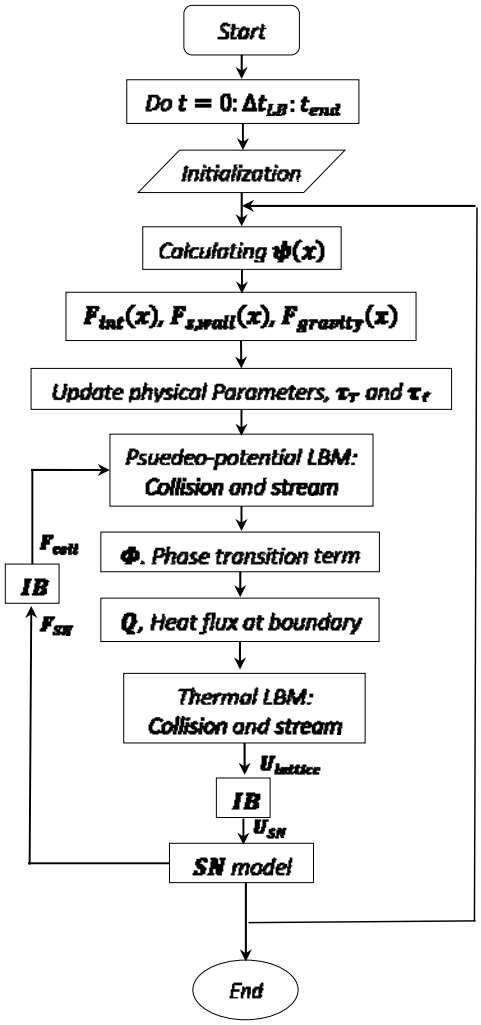

Fig. 11. Solution process flow chart.

After initialization, a thermal pulse of $8 \times 10^6 W.m^{-2}$ for $4\mu s$ is applied to the heater element. It should be mentioned that during injection process, temperature dependent physical properties such as thermal diffusivity and viscosity, see Table 1, are constantly being updated thorough relaxation parameters. Moreover, the relevant value for water thermal conductivity and specific heat at different temperatures are also listed in Table 2. The simulation time step in physical unit is 3.5ns.

Table 2. Water thermal conductivity and specific heat at different temperatures.

T	k_l $(W.m^{-1}.K^{-1})$	k_v $(W.m^{-1}.K^{-1})$	$C_{p,l}$ $(KJ.kg^{-1}.K^{-1})$	$C_{p,v}$ $(KJ.kg^{-1}.K^{-1})$
$0.5T_c$	*0.64*	*0.02*	*4.17*	*1.94*
$0.6T_c$	*0.68*	*0.026*	*4.23*	*2.14*
$0.7T_c$	*0.67*	*0.049*	*4.40*	*2.41*
$0.8T_c$	*0.627*	*0.06*	*4.80*	*3.84*

The time sequence of nucleation, bubble growth, droplet ejection and bubble collapse processes are demonstrated in Fig. 12. Furthermore, the temperature distribution at different times are also shown in Fig. 13. Videos of this process are also made available as supplementary material to this paper which can provide a better understanding of rapid explosive droplet injection process [48]. Supplementary Video 1 demonstrates density distribution during droplet

ejection process while Supplementary video 2 displays temperature distribution changes at any instance of time. At the beginning stage of thermal pulse, the temperature of water in contact with heater element is increasing relatively slow. However, right before heat flux stops, the temperature of lattice nodes on lower boundary drastically increase as shown in Fig. 13. For instance, the temperature of nodes on heater element just before the end of heat pulse is $\approx 1.5T_c$. However, bubbles only start to form $2\mu s$ after heat pulse stops as shown in Fig. 12. In normal boiling situation, small vapor and gas bubble trapped in cracks act as a preexisting nuclei. In inkjet printing, bubbles are generated at superheated temperatures. Thus, temperature distribution on the heater is the most important factor directly influencing bubble nucleation. Since the length of heater pad is twice as big as its width, there is two places with maximum local temperature at initial stages of simulation, see Fig. 13. These two local maxima are the main reason that derive the formation of two bubbles instead of one. These two nucleated bubbles gradually grow and eventually aggregate to form one big bubble as it pushes water droplet out of nozzle. It should be noted that vapor is in its saturated state and +will ultimately collapse as heat dissipate to surrounding liquid. During $4\mu s$ collapse cycle, bubble quickly disappear when it reaches its maximum volume at $t = 31\mu s$ as shown in Fig. 14.

As discussed before, reduced parameter is assumed to linearly increase with temperature. Bigger values for reduced parameter drastically increases spurious current and ultimately result in solution divergence. On the other hand, we could potentially use smaller reduced parameters. However, we needed to use significantly finer mesh.

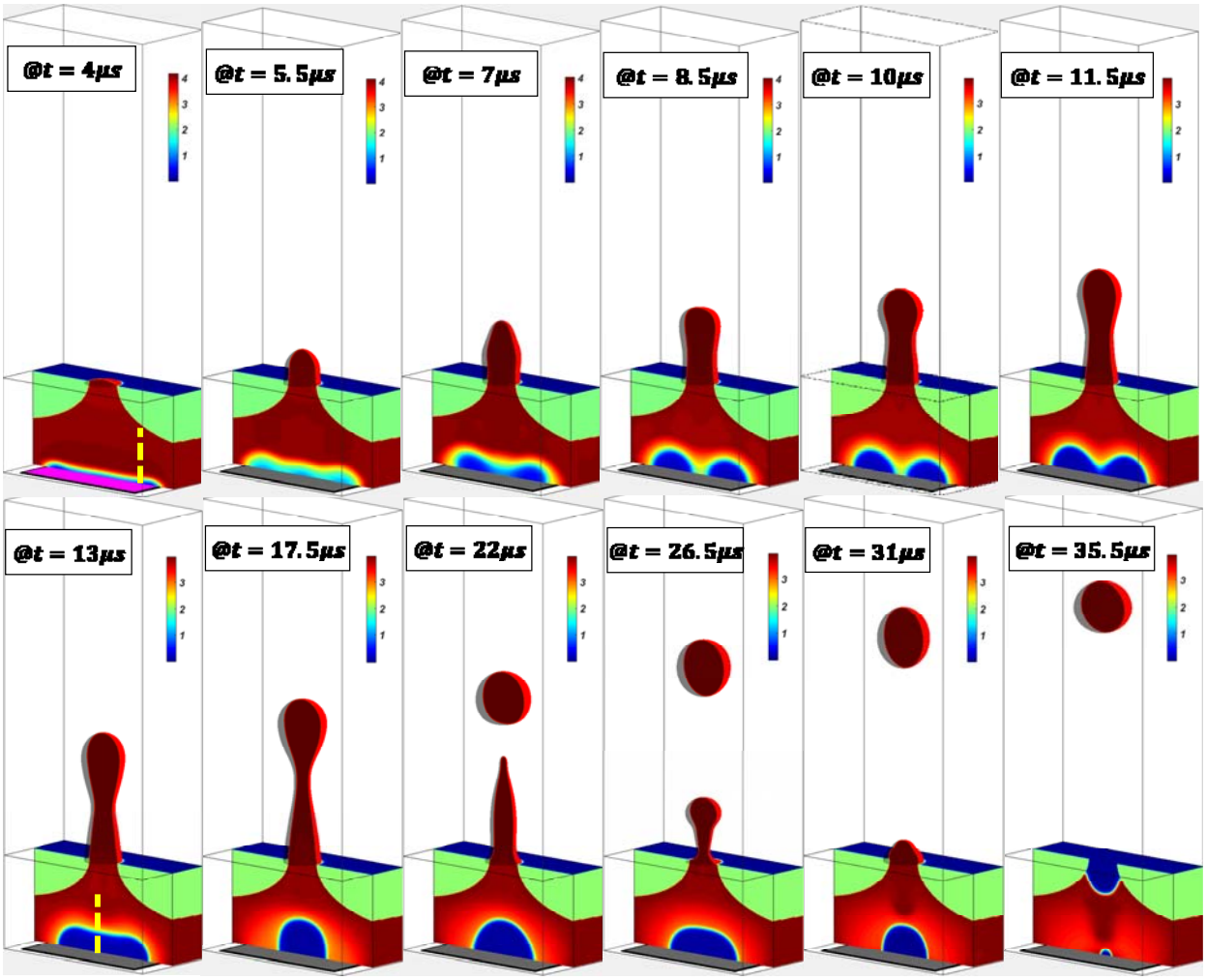

Fig. 12. Time sequence of droplet injection process at nozzle cross section. Color bar represents relative density.

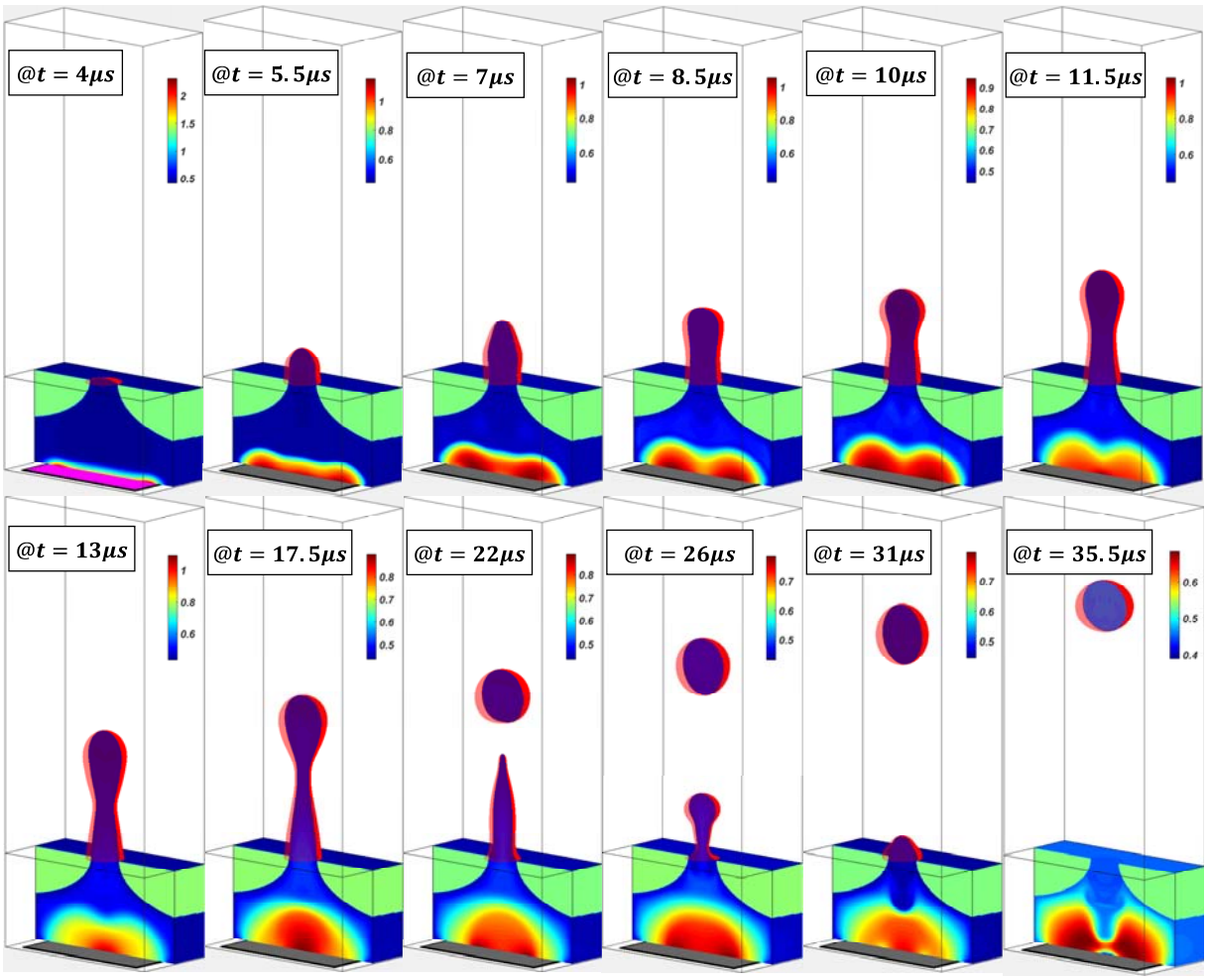

Fig. 13. Time sequence of droplet injection process at nozzle cross section. Color bar represents relative temperature.

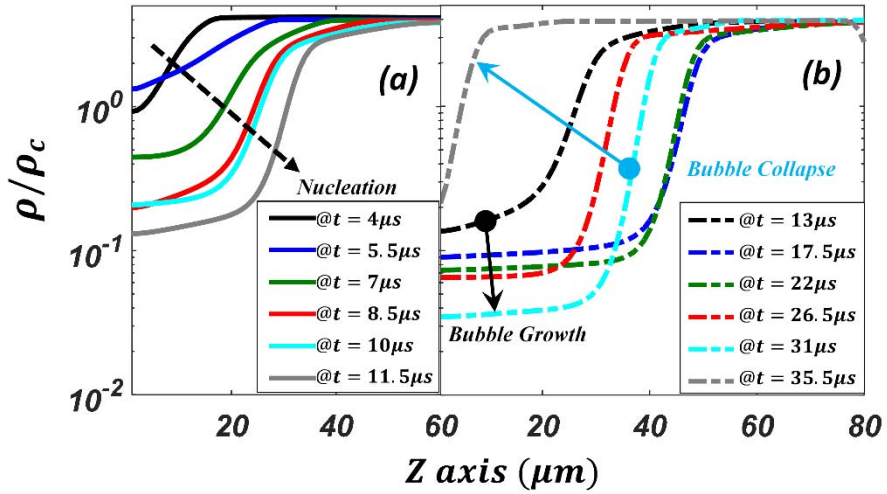

Fig. 14. Relative density distribution during nucleation, bubble growth and bubble collapse (a) before and (b) after bubble coalescence. The density data shown are related to dashed lines shown in Fig. 12 at (a) and (b) . In (a), black and grey solid lines represent density distribution at and , respectively. In (b), black and grey dashed lines represent density distribution at and , respectively.

The final speed of projectile is approximately which agrees with previous numerical and experimental studies [13, 17, 45, 46]. The drop head velocity at any instance of time is depicted in Fig. 15 where it is compared with experimental measurement and CFD modeling of Tan et al. [45]. Drophead velocity is directly linked to Bubble expansion rate. Most researchers normally adopt the Clausius–Clapeyron equation to predict bubble growth [16, 49]. However, Tan et al [45] utilized polytropic gas expansion to avoid using an additional thermal model to solve the temperature distribution. Regardless of this simplification, drophead velocity from their simulation matched well with experiment. Since bubble explosive expansion happens in a few microseconds, the expansion rate and therefore drophead velocity may not be very different between these models. Another important parameter influencing drophead velocity is the nozzle geometry. Zhou and Gue [16] showed that chamber and nozzle geometry will play an important role in projectile speed. Smaller the nozzle diameter, higher the drophead velocity would be. The nozzle diameter in Tan et al. study [45] is while in our study it was . Their printhead geometry cannot be utilized for bioprinting because it nozzle diameter is small for injecting cells, . Moreover, the geometry of their printhead is significantly more complicated compared to HP60. Although different print head geometry is used in our simulation, it is observed that our numerical results roughly matches the experimental result and CFD simulation of Tan et al. [45]. The main reason for lower printhead velocity is using nozzle with bigger diameter, , compared to Tan et al. work [45] where it was .

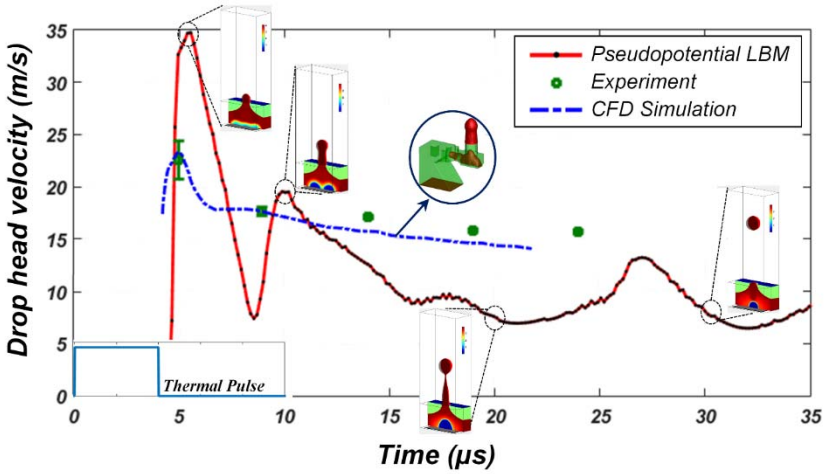

Fig. 15. Comparison of drop head velocity between experiment [45], CFD simulation of Tan et al. [45], and pseudopotential LB method in this study.

Evidently, the temperature distribution is not uniform inside the saturated bubble. Thus, vapor density would be different in various locations of affected region and it is constantly changing by time. Moreover, due to continuous fluid motion, the pressure is also not uniform inside the chamber. The time history of minimum vapor density, maximum temperature and maximum local pressure in the chamber are demonstrated in Fig. 16a, Fig. 16b and Fig. 17, respectively. Due to high heat flux, the maximum local pressure, maximum temperature and minimum vapor density in most critical location of nucleated bubble instantly reach to highest values of , and , respectively. Thus, the vapor thermodynamic state in nucleated bubble is very close to water critical point.

Furthermore, during bubble expansion, pressure, temperature and density continuously decrease as shown in Fig. 16 and Fig. 17. When bubble reaches it maximum volume, the pressure energy has already converted to kinetic energy. As heat dissipate to surrounding liquid, the saturated vapor pressure gradually decreases resisting liquid water refilling bubble. Finally, during collapse stage, the maximum local pressure drastically decreases and bubble rapidly disappear in just . Although previous CFD studies [13, 45], did a nice job simulating ejection dynamic, they lack

a realistic bubble model. For instance, the maximum bubble pressure in Tan's model [13] is while we predict instantaneous saturated pressure as high as which is closer to previously reported values of in Ref. [16]. To discuss this in more detail, Asai et al. [50] reported that the saturated vapor pressure will reach 10~100 times as high as the atmospheric pressure. In their later study [51, 52], initial bubble pressure was taken 7.5Mpa. It should be noted that bubble generation and collapse happen very fast and vapor close to heating element is saturated during this period. Thus, the maximum bubble pressure should be at least 7.5Mpa (saturated vapor pressure of water at) during nucleation. A recent study [17] used similar logic to assume an initial vapor pressure as an input to their model.

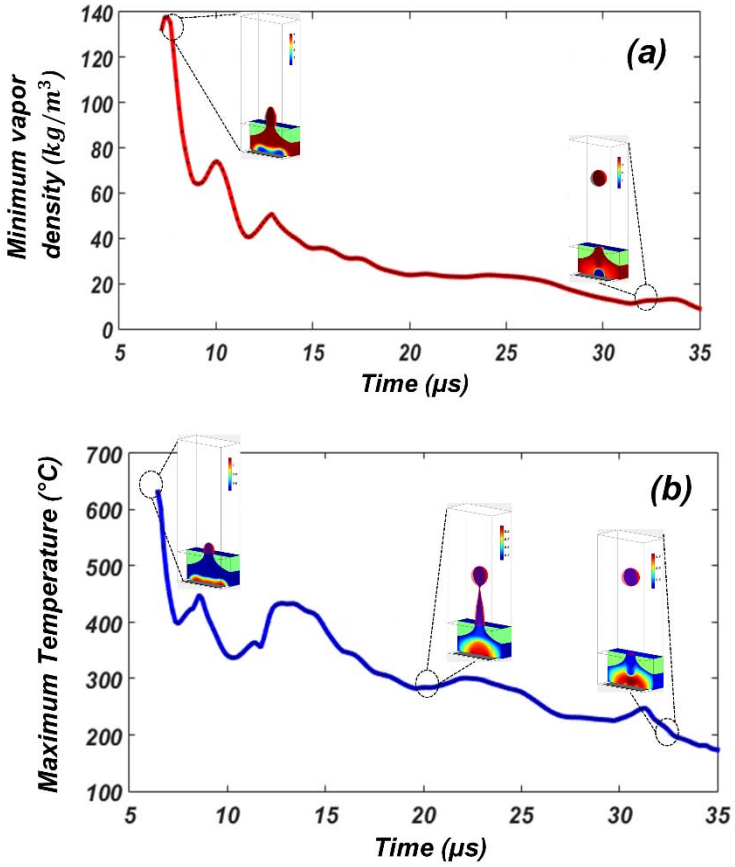

Fig. 16. The history of (a) minimum vapor density and (b) maximum local temperature from pseudopotential LB method.

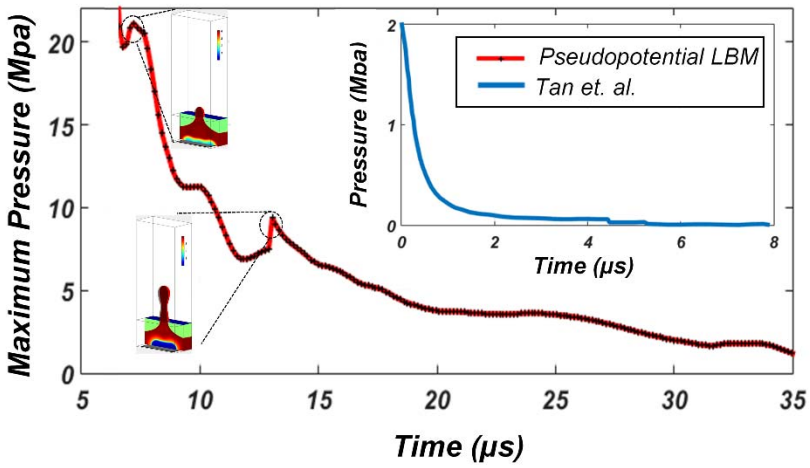

Fig. 17. Maximum local pressure derived from pseudopotential LB method in this study compared to vapor pressure used in [13].

Compared to previous studies, inclusion of compressibility effect via direct implementation of EOS and phase transition using pseudopotential LBM and heat conduction through thermal LBM, all in one setup, makes our modeling more realistic. These features distinct our modeling approach from previous conventional CFD methods where vapor bubble was merely treated as a cavity [13, 16, 45-47]. Easy implementation of various models in one platform is one other advantage of current method. Furthermore, easy parallelization of LBM code can also significantly enhance computation speed.

5. Cell damage

Thermal inject has been successfully used for printing cells, yet potential cell damage is hard to be evaluated in experiments [14, 24, 25, 53, 54]. To study membrane mechanical damage, cell deformation squeezing out of nozzle head is needed to be visualized first. To model bio-printing process, the cell membrane in its natural state is modeled as a floating sphere with diameter of It consist of vertex nodes connected by linear spring with stiffness of . Moreover, the triangular network has bending stiffness, local area constraint stiffness, global area constraint stiffness and volume constraint stiffness of , , and , respectively. During rapid explosive vapor expansion, the cell squeezes out of nozzle and quickly reaches its most deformed state at as shown in Fig. 18. In the following, we briefly discuss cell deformation/damage during thermal injection process.

Cui et. al. experimentally investigated the viability and pore development on membrane of printed Chinese hamster ovary cells [24]. They used propidium iodide and dextran molecules of various molecular weights to stain the printed cells. Then, they evaluated the cutoff molecular size of these agent penetrating cell membrane. By doing that, they would be able to estimate pore size and better understand transient nature of pores after printing. Measuring fluorescence intensity of stained cells after , they confirmed existence of size pores on cell membrane. They also reported that the pore size gradually decreases by time and they completely disappear after hours incubation.

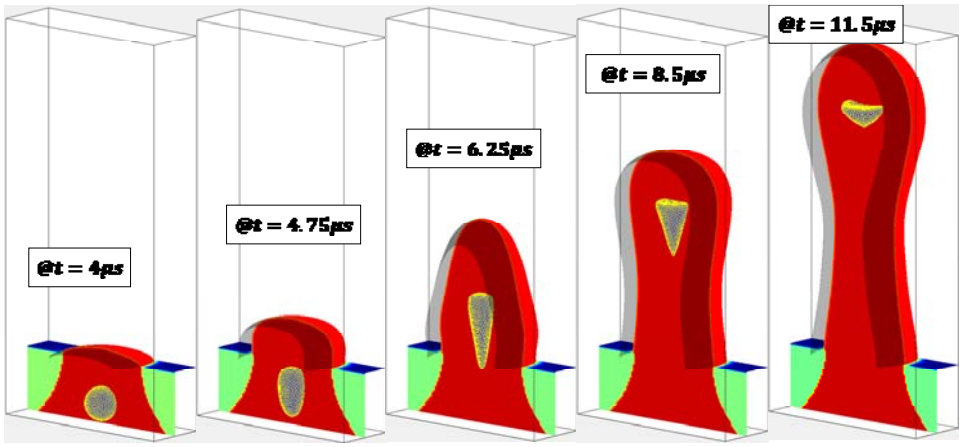

Fig. 18. Time sequence of cell deformation as it get squeezed out of nozzle printer.

Cells damage during printing process can be associated with thermal shock or mechanical deformation. According to our study, temperature rise to critical temperatures is mostly maintained within vaporous region close to heating element and cells floating in the solution may rarely come in contact with this high temperature zone. Additionally, pore formation on cell membrane can be directly attributed to mechanical damage [24]. The transient nature of formed pores on cell membrane suggest that mechanical deformation is the reason for the damage.

On important factor which strongly influence mechanical resistance of cell membrane is loading speed. Koshiyama and Wada [55] carried out numerical simulations studying pore formation dynamics under various loading condition. They specifically focused on effect of stretching speeds on pore formation process. They performed equibiaxial stretching simulations on a bilayer patch with pulling speeds of 0.1, 0.3 and 1.0 $m.s^{-1}$. Their molecular dynamic simulation results indicated that multi-pores are more likely to form under higher stretching speeds. Pore formation under mechanical loading at the molecular level is a statistical phenomenon. Thus, Koshiyama and Wada [55] present their results for the average chance of pore formation as a function of areal strain using error function. For instance, at certain stretching speed and areal strain, we can look up probability of pore formation as shown in Fig. 19e. For more detail information on this topic, readers can refer to our previous work [33] where we studied mechanical damage of red blood cell membrane under high shear flows.

Under quasi-static loading condition, we will have 100% pore formation at areal strain 1.2 and progressive pore growth on cell membrane will eventually lead to cell rupture, see Fig. 19e. However, at higher loading speed, the pores start to form at much higher areal strain. Thus, to further study mechanical deformation leading to pore formation, we analyze membrane deformation at its most stretched state. Areal strain, stretching speed, maximum axial stress and maximum shear stress distribution on cell membrane is plotted at $6.25\mu s$ in Fig. 19a-d. It is observed that areal strain can reaches 0.85 during very short period of time under high loading speed of 0.2 m/s. Equibiaxial stretching assumption is used for the calculation of this loading speed [55]. However, the stretching speed in critical direction can even reach 1.5 m/s. In this condition, the maximum areal strain of membrane falls well below critical threshold, proving that cells are most likely to survive printing process. Even for cases with smaller nozzles, cell viability won't drop significantly as long as the maximum areal strain is maintained below the acceptable range. Moreover, according to Koshiyama and Wada study [55] at these high deformation/loading speed, the squeezing energy will be release through creation of multiple smaller pores rather than one bigger pore [55]. Thus, increase in loading rate will result in increase in rupture tension [56]. In other word, high loading rate retards formation of big pores and accordingly the cell rupture [57].

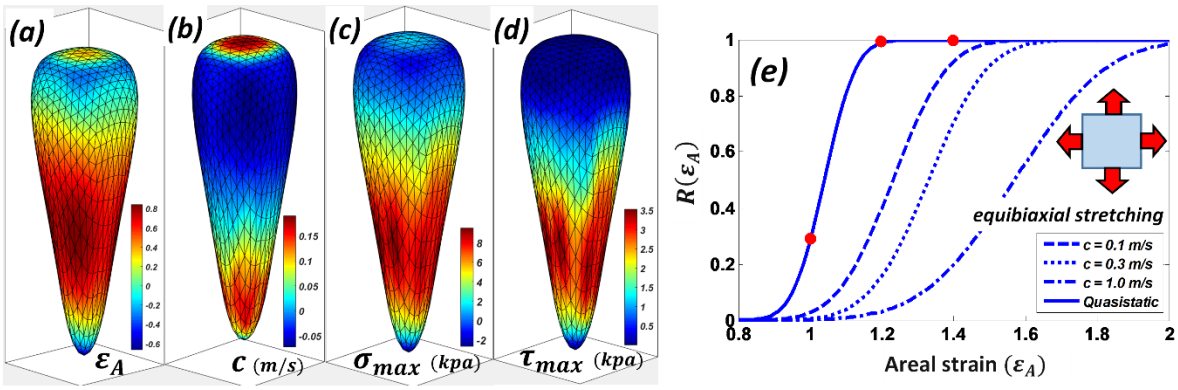

Fig. 19. (a) areal strain, (b) stretching speed, (c) maximum axial stress and (d) maximum shear stress distribution on cell membrane at . (e) The probability of pore formation at various stretching speeds [55].

6. Conclusions

Pseudopotential LBM is well capable of modeling phase transition. However, it is unstable at ambient temperature. Due to this limitation, the pseudopotential thermal LBM has not yet been applied to complex phase changing applications at ambient temperature. We proposed a novel approach which utilize temperature dependent reduced parameters to overcome this limitation. It allows us look into instantaneous phase change phenomena with local high temperature gradient which has not been done before to the best of our knowledge. Using this method, we are also able to concurrently simulate heat transfer, phase transition and fluid-cell interaction in one platform. While previous thermal ejection simulations treat bubble vapor artificially as a cavity, vapor and liquid densities in our approach are directly linked to temperature and pressure in a physical way through non-ideal EOS and the only input to computational domain is the heat pulse at lower boundary. Furthermore, all temperature dependent fluid properties are also constantly being updated during the simulation. Overall, we showed that we simulate bubble nucleation/growth more realistically. Furthermore, our simulation is capable to study whether and how mechanical or heat shock will damage cells in bio-printing. To model bio-printing process, we coupled our modified Pseudopotential thermal LBM formulation with spring network model through immersed boundary method. Cell deformation is visualized as it squeezes out of nozzle head. It was observed that that fast deformation of cell membrane can significantly increase rupture tension. The novelties of this study can be summarized as:

1. Introduce and utilize a temperature dependent reduced parameter to stabilize pseudopotential method at room temperature.
2. Simulate various phenomena such as phase transition, heat transfer, cell deformation, and wall-liquid interaction in one platform.
3. Present a more realistic simulation of bubble nucleation, growth, and collapse by directly implementing non-ideal EOS of water into LBM formulation.
4. Provide better insights into mechanical damage of cell membrane during drop-on demand cell printing process.

For future work, pseudopotential model can be used in conjunction with adaptive mesh method to minimize interface thickness. We also encounter some instability difficulties which can be probably avoided by using multi-relaxation method in future.

Acknowledgement

The authors acknowledge the supports of this work from the National Science Foundation (NSF) CAREER grant CBET-0955214 and the National Institute of Health (NIH) grant EB015105.

Reference

[1] Sohrabi, S., Saidi, M.S., Saadatmand, M., Banazadeh, M.H., Firoozabadi, B. Three-dimensional simulation of urine concentrating mechanism in a functional unit of rat outer medulla. I. Model structure and base case results. Mathematical biosciences 258:44-56 (2014).
[2] Sohrabi, S., Wang, S., Tan, J., Xu, J., Yang, J., Liu, Y. Nanoparticle transport and delivery in a heterogeneous pulmonary vasculature. Journal of Biomechanics 50:240-247 (2017).
[3] Wang, S., Sohrabi, S., Xu, J., Yang, J., Liu, Y. Geometry design of herringbone structures for cancer cell capture in a microfluidic device. Microfluidics and Nanofluidics 20:148 (2016).
[4] Rajabzadeh-Oghaz, H., Varble, N., Davies, J.M., Mowla, A., Shakir, H.J., Sonig, A., et al.: Computer-assisted adjuncts for aneurysmal morphologic assessment: toward more precise and accurate approaches. Medical Imaging 2017: Computer-Aided Diagnosis, pp. 101341C. International Society for Optics and Photonics, Place International Society for Optics and Photonics (2017)
[5] Yuan, P., Schaefer, L. Equations of state in a lattice Boltzmann model. Physics of Fluids 18:042101 (2006).
[6] Fakhari, A., Bolster, D., Luo, L.-S. A weighted multiple-relaxation-time lattice Boltzmann method for multiphase flows and its application to partial coalescence cascades. Journal of Computational Physics 341:22-43 (2017).
[7] Hu, A., Li, L., Chen, S., Liao, Q., Zeng, J. On equations of state in pseudo-potential multiphase lattice Boltzmann model with large density ratio. International Journal of Heat and Mass Transfer 67:159-163 (2013).
[8] Gong, S., Cheng, P. Numerical investigation of droplet motion and coalescence by an improved lattice Boltzmann model for phase transitions and multiphase flows. Computers & Fluids 53:93-104 (2012).
[9] Shan, X., Chen, H. Lattice Boltzmann model for simulating flows with multiple phases and components. Physical Review E 47:1815 (1993).
[10] Swift, M.R., Osborn, W., Yeomans, J. Lattice Boltzmann simulation of nonideal fluids. Physical Review Letters 75:830 (1995).
[11] Fakhari, A., Geier, M., Bolster, D. A simple phase-field model for interface tracking in three dimensions. Computers & Mathematics with Applications (2016).
[12] Kupershtokh, A., Medvedev, D., Karpov, D. On equations of state in a lattice Boltzmann method. Computers & Mathematics with Applications 58:965-974 (2009).
[13] Tan, H. An adaptive mesh refinement based flow simulation for free-surfaces in thermal inkjet technology. International Journal of Multiphase Flow 82:1-16 (2016).
[14] Wilson, W.C., Boland, T. Cell and organ printing 1: protein and cell printers. The Anatomical Record 272:491-496 (2003).
[15] Lee, S.-W., Kim, H.-C., Kuk, K., Oh, Y.-S. A monolithic inkjet print head: DomeJet. Sensors and Actuators A: Physical 95:114-119 (2002).
[16] Zhou, H., Gué, A. Simulation model and droplet ejection performance of a thermal-bubble microejector. Sensors and Actuators B: Chemical 145:311-319 (2010).
[17] Suh, Y., Son, G. A level-set method for simulation of a thermal inkjet process. Numerical Heat Transfer, Part B: Fundamentals 54:138-156 (2008).
[18] Ruiz, O.: CFD model of the thermal inkjet droplet ejection process. ASME/JSME 2007 Thermal Engineering Heat Transfer Summer Conference collocated with the ASME 2007 InterPACK Conference,

pp. 357-365. American Society of Mechanical Engineers, Place American Society of Mechanical Engineers (2007)
[19] Lindemann, T., Sassano, D., Bellone, A., Zengerle, R., Koltay, P., Olvetti, I.: Three-dimensional CFD-simulation of a thermal bubble jet printhead. NSTI nanotechnology conference and trade show, pp. 227-230. Place (2004)
[20] Nikolopoulos, N., Nikas, K.-S., Bergeles, G. A numerical investigation of central binary collision of droplets. Computers & Fluids 38:1191-1202 (2009).
[21] Lee, W., Son, G. Numerical study of droplet impact and coalescence in a microline patterning process. Computers & Fluids 42:26-36 (2011).
[22] Rajabzadeh-Oghaz, H., Firoozabadi, B., Saidi, M.S., Monjezi, M., Shirazi, M.A.N., Rad, E.M. Pulsatile blood flow in total cavopulmonary connection: a comparison between Y-shaped and T-shaped geometry. Medical & biological engineering & computing 55:213-224 (2017).
[23] Forughi, A., Green, S., Stoeber, B. Optical transparency of paper as a function of moisture content with applications to moisture measurement. Review of Scientific Instruments 87:023706 (2016).
[24] Cui, X., Dean, D., Ruggeri, Z.M., Boland, T. Cell damage evaluation of thermal inkjet printed Chinese hamster ovary cells. Biotechnology and bioengineering 106:963-969 (2010).
[25] Roth, E.A., Xu, T., Das, M., Gregory, C., Hickman, J.J., Boland, T. Inkjet printing for high-throughput cell patterning. Biomaterials 25:3707-3715 (2004).
[26] Cui, X., Boland, T., D D'Lima, D., K Lotz, M. Thermal inkjet printing in tissue engineering and regenerative medicine. Recent patents on drug delivery & formulation 6:149-155 (2012).
[27] Liu, W.K., Liu, Y.L., Farrell, D., Zhang, L., Wang, X.S., Fukui, Y., et al. Immersed finite element method and its applications to biological systems. Comput Method Appl M 195:1722-1749 (2006).
[28] Tan, J., Wang, S., Yang, J., Liu, Y. Coupled particulate and continuum model for nanoparticle targeted delivery. Comput Struct 122:128-134 (2013).
[29] Sohrabi, S., Zheng, J., Finol, E.A., Liu, Y. Numerical Simulation of Particle Transport and Deposition in the Pulmonary Vasculature. Journal of biomechanical engineering 136:121010 (2014).
[30] Gong, S., Cheng, P. Lattice Boltzmann simulation of periodic bubble nucleation, growth and departure from a heated surface in pool boiling. International Journal of Heat and Mass Transfer 64:122-132 (2013).
[31] Guo, Z., Shi, B., Zheng, C. A coupled lattice BGK model for the Boussinesq equations. International Journal for Numerical Methods in Fluids 39:325-342 (2002).
[32] Gong, S., Cheng, P. A lattice Boltzmann method for simulation of liquid–vapor phase-change heat transfer. International Journal of Heat and Mass Transfer 55:4923-4927 (2012).
[33] Sohrabi, S., Liu, Y. A Cellular Model of Shear‐Induced Hemolysis. Artificial Organs (2016).
[34] Fedosov, D., Caswell, B., Karniadakis, G.E.: Coarse-grained red blood cell model with accurate mechanical properties, rheology and dynamics. Engineering in Medicine and Biology Society, 2009 EMBC 2009 Annual International Conference of the IEEE, pp. 4266-4269. IEEE, Place IEEE (2009)
[35] Fedosov, D.A., Fornleitner, J., Gompper, G. Margination of white blood cells in microcapillary flow. Physical review letters 108:028104 (2012).
[36] Ujihara, Y., Nakamura, M., Miyazaki, H., Wada, S. Proposed spring network cell model based on a minimum energy concept. Annals of biomedical engineering 38:1530-1538 (2010).
[37] Fedosov, D.A., Caswell, B., Karniadakis, G.E. A multiscale red blood cell model with accurate mechanics, rheology, and dynamics. Biophysical journal 98:2215-2225 (2010).
[38] Ujihara, Y., Nakamura, M., Miyazaki, H. Effects of the initial orientation of actin fibers on global tensile properties of cells. Journal of Biomechanical Science and Engineering 5:515-525 (2010).
[39] Peskin, C.S. The immersed boundary method. Acta numerica 11:479-517 (2002).

[40] Peskin, C.S., McQueen, D.M. A three-dimensional computational method for blood flow in the heart I. Immersed elastic fibers in a viscous incompressible fluid. Journal of Computational Physics 81:372-405 (1989).
[41] Tan, J., Keller, W., Sohrabi, S., Yang, J., Liu, Y. Characterization of Nanoparticle Dispersion in Red Blood Cell Suspension by the Lattice Boltzmann-Immersed Boundary Method. Nanomaterials 6:30 (2016).
[42] Abkarian, M., Faivre, M., Viallat, A. Swinging of red blood cells under shear flow. Physical review letters 98:188302 (2007).
[43] Zou, Q., He, X. On pressure and velocity boundary conditions for the lattice Boltzmann BGK model. Physics of fluids 9:1591-1598 (1997).
[44] Zou, Q.S., He, X.Y. On pressure and velocity boundary conditions for the lattice Boltzmann BGK model. Phys Fluids 9:1591-1598 (1997).
[45] Tan, H., Torniainen, E., Markel, D.P., Browning, R.N. Numerical simulation of droplet ejection of thermal inkjet printheads. International Journal for Numerical Methods in Fluids 77:544-570 (2015).
[46] Sen, A., Darabi, J. Droplet ejection performance of a monolithic thermal inkjet print head. Journal of micromechanics and microengineering 17:1420 (2007).
[47] Yang, A.-S., Tsai, W.-M. Ejection process simulation for a piezoelectric microdroplet generator. Journal of fluids engineering 128:1144-1152 (2006).
[48] See Supplemental Material at [URL will be inserted by publisher] for a short video demonstrating density distribution during droplet ejection process.
[49] Hong, Y., Ashgriz, N., Andrews, J., Parizi, H. Numerical simulation of growth and collapse of a bubble induced by a pulsed microheater. Journal of microelectromechanical systems 13:857-869 (2004).
[50] Asai, A., Hara, T., Endo, I. One-dimensional model of bubble growth and liquid flow in bubble jet printers. Japanese Journal of Applied Physics 26:1794 (1987).
[51] Asai, A. Three-dimensional calculation of bubble growth and drop ejection in a bubble jet printer. TRANSACTIONS-AMERICAN SOCIETY OF MECHANICAL ENGINEERS JOURNAL OF FLUIDS ENGINEERING 114:638-638 (1992).
[52] Asai, A. Application of the nucleation theory to the design of bubble jet printers. Japanese Journal of Applied Physics 28:909 (1989).
[53] Cui, X., Boland, T. Human microvasculature fabrication using thermal inkjet printing technology. Biomaterials 30:6221-6227 (2009).
[54] Xu, T., Gregory, C.A., Molnar, P., Cui, X., Jalota, S., Bhaduri, S.B., et al. Viability and electrophysiology of neural cell structures generated by the inkjet printing method. Biomaterials 27:3580-3588 (2006).
[55] Koshiyama, K., Wada, S. Molecular dynamics simulations of pore formation dynamics during the rupture process of a phospholipid bilayer caused by high-speed equibiaxial stretching. Journal of biomechanics 44:2053-2058 (2011).
[56] Shigematsu, T., Koshiyama, K., Wada, S. Effects of Stretching Speed on Mechanical Rupture of Phospholipid/Cholesterol Bilayers: Molecular Dynamics Simulation. Scientific reports 5 (2015).
[57] Evans, E., Heinrich, V., Ludwig, F., Rawicz, W. Dynamic tension spectroscopy and strength of biomembranes. Biophysical journal 85:2342-2350 (2003).